


Article

Aerodynamic Optimization and Mechanism Investigation on Performance Improvements in a Transonic Compressor Cascade

Fanjie Meng , Chaoxuan Gong, Kunhang Li, Jin Xiong, Jingyin Li *  and Penghua Guo

School of Energy and Power Engineering, Xi'an Jiaotong University, West Xianning Road, Xi'an 710049, China
* Correspondence: jyli@mail.xjtu.edu.cn

Abstract: In this paper, a transonic compressor cascade was optimized to improve its aerodynamic performance. A new blade parameterization method with 16 control variables was first proposed to fit the shapes of the suction and the pressure side, as well as the leading edge. Then, the Kriging surrogate-model-based genetic algorithm (GA) was used to optimize the performance of the transonic cascade. The optimization algorithm is effective in reducing the total pressure loss while extending the working range of the cascade. The results show that the total pressure loss coefficient could be reduced by 11% at the best airflow angle and the working range could be extended by 6.9% for the optimized cascade in two-dimensional simulations. Similar improvement results could also be obtained in the simulations of their linear cascade cases. Detailed analyses show that the relative maximum thickness positions of the optimized blades move forward by about 10% to the leading edge, and the radii of curvature of the front half of the suction and pressure surfaces increase, compared with the initial blade. This makes the front half of the optimized blades look more closely like a wedge. Consequently, the passage shock strength is reduced and the shock changes from the passage normal shock to oblique shock. The weakened shock strength leads to the disappearance of the flow separation caused by the shock boundary layer interaction on the suction surfaces of the optimized blades, and results in a narrowed wake width at the outlet section.

Keywords: transonic compressor cascade; optimization design; shock control; shock wave boundary layer interaction



Citation: Meng, F.; Gong, C.; Li, K.; Xiong, J.; Li, J.; Guo, P. Aerodynamic Optimization and Mechanism Investigation on Performance Improvements in a Transonic Compressor Cascade. *Machines* **2023**, *11*, 244. <https://doi.org/10.3390/machines11020244>

Academic Editors: Kim Tiow Ooi and Davide Astolfi

Received: 21 December 2022

Revised: 19 January 2023

Accepted: 30 January 2023

Published: 7 February 2023



Copyright: © 2023 by the authors. Licensee MDPI, Basel, Switzerland. This article is an open access article distributed under the terms and conditions of the Creative Commons Attribution (CC BY) license (<https://creativecommons.org/licenses/by/4.0/>).

1. Introduction

The transonic axial flow compressor is one of the three key components of a heavy-duty gas turbine, and its aerodynamic performance is closely related to the characteristics of the whole machine. The high stage pressure ratio requirement presents new challenges to the design of transonic axial flow compressors [1]. Therefore, understanding the flow features around transonic cascades is required for the design of a transonic stage with a high efficiency and a wide working range. Although the actual flow inside the compressor is three-dimensional (3D), the transonic cascade data are still very helpful for exploring the underlying mechanism for the losses and flows in the transonic compressor stages.

Unlike the common subsonic cascades, transonic cascades have two special sources of loss: the shock loss caused by the presence of shock waves and the flow loss caused by the shock boundary layer interaction (SBLI) [2]. Therefore, controlling the flow losses caused by shocks and the SBLI are the major concerns of transonic compressor cascades. Many methods have been proposed to suppress the losses due to shock waves. For the flow control approaches, they can be divided into two categories: the active control [3,4], such as the surface suction or blowing, and the passive control [5,6], such as the vortex generator or the slotting method. In practice, a convenient way to control the shock wave pattern and strength is to optimize the blade shape, because the shock loss is very sensitive to the change in the blade profile. For example, Mazaheri and Khatibirad [7] reduced the total pressure loss by adding a shock control bump (SCB) to the NASA rotor 67 blade

section. A multi-point and two single-point optimizations were performed in the design and off-design conditions. The results show that the single-point optimized shape has the best performance at the operating point, while the multi-point optimized shape has better overall performance over the whole working range. A similar approach was adopted by Jinks et al. [8] for the optimal design of an adaptive shock control bump on the transonic airfoil surface. Furthermore, according to the research of Refs. [9–11], the leading edge of the blade has an important effect on the profile loss of the transonic compressor cascade. Although the shape of the suction surface plays an important role in the flow losses of the transonic blade, the SCB method does not take into account the profile loss and shock loss caused by the variations in the profiles of the leading edge and the pressure surface, which also are important influencing factors.

Historically, the design of a blade shape can generally be divided into four main categories [12]: The first one is represented by C4 airfoil, NACA65 airfoil and BC6 airfoil, all of which have parabolic mean camber lines. The second one has a double-arc and multi-circular-arc profiles. The third type has controlled diffusion airfoil [13]. For the fourth type, the blade shape is designed by using the aerodynamic shape parameterization methods, such as class shape transformation [14], free deformation methods [15] and adjoint-based shape optimization [16]. The optimization of blade profiles by altering the control points of the blade shape parameterization has attracted much attention in the past decades, while the computational fluid dynamic (CFD) approach has found wide application in analyzing flow fields. The often-used blade shape parameterization methods are the ones to determine the camber line and thickness distribution [17,18], and the ones to generate the suction and the pressure surface profile [19,20]. For example, Ju and Zhang [21] optimized a compressor cascade from an industrial axial flow compressor by using a multi-point, multi-objective optimization design method to extend the working range of the cascade while maintaining good performance. Venturelli and Benini [22] optimized an S-shape supersonic cascade by using the second parameterization approach. Presently, the CFD method is capable of making a reasonable prediction of the separation flow and the vortex shedding frequency [23,24]. Therefore, the CFD method lay a reliable foundation for the parameterization optimization based on the direction computational method, especially for the multi-point and multi-objective aerodynamic optimization.

The present optimization of blade shape using the blade parameterization method needs a large number of expensive CFD simulations. Researchers proposed to use the surrogate model in the optimization framework [25,26], to save the cost of CFD computations. Consequently, many surrogate models have been proposed and developed, such as the polynomial regression model, Kriging model, support vector machine and artificial neural network. The examples, to cite a few, include the design and optimization of a compressor tandem cascade by using an artificial neural network [27], and the optimization of a compressor cascade using support vector regression [28]. The results of the above examples showed an evident improvement in the performance of a compressor cascade and significantly reduced CFD expenditure in the meantime.

The experimental data on a cascade derived from a rotor blade section of a real transonic compressor are scarce, because the requirement for such an experimental rig is very high, such as the need for a high power supply, a large space and the expensive specific equipment for the cascade wind tunnel. In this paper, a new blade parameterization method is proposed for a transonic compressor cascade, to control the blade profile including the leading edge, the suction and the pressure surface. To minimize the total pressure loss and extend the working range of the cascade, a Kriging surrogate-model-assisted genetic algorithm (GA) optimization method was applied to optimize the aerodynamic performance of a transonic cascade derived from an industry compressor. The underlying mechanisms for the reduction in flow losses are also explored by analyzing the variations in flow fields in detail.

2. Cascade Modeling and Numerical Method

2.1. Compressor Cascade

In this paper, the geometry of the transonic compressor cascade under investigation is shown in Figure 1. The data of the linear cascade under investigation are listed in Table 1. The blade profile of the transonic cascade was scaled from the blade section of the first rotor of the axial flow compressor in a heavy-duty gas turbine. The aerodynamic experiment was carried out at inlet Mach number $Ma_1 = 0.9$ in a wind tunnel for linear cascades at Dalian Maritime University. For a detailed description of the test equipment and measurements, please refer to Ref. [29].

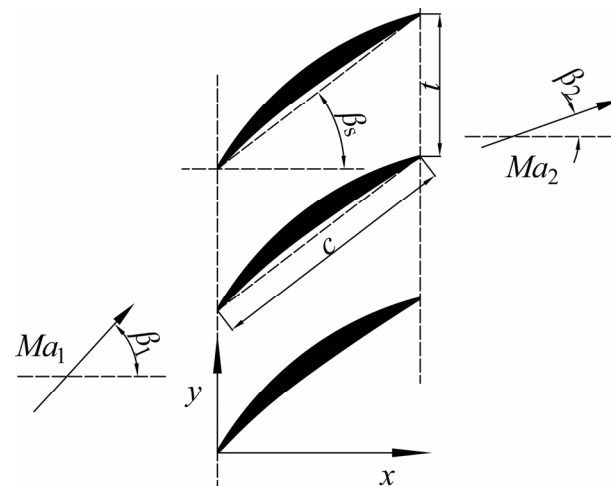


Figure 1. Diagram of cascade geometric parameters.

Table 1. Transonic compressor cascade parameters.

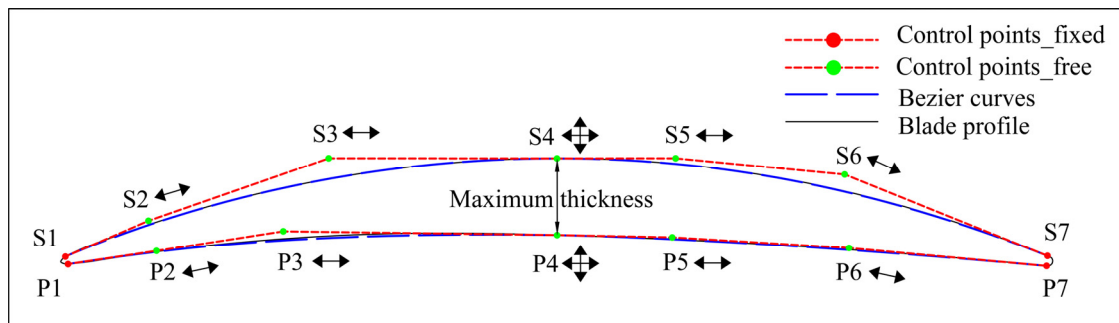
Parameters	Value
Chord length c	47.15 mm
Pitch length t	32.63 mm
Solidity c/t	1.44
Span length s	100 mm
Stagger angle β_s	37.46 deg
Camber angle	27.46 deg

2.2. Cascade Modeling

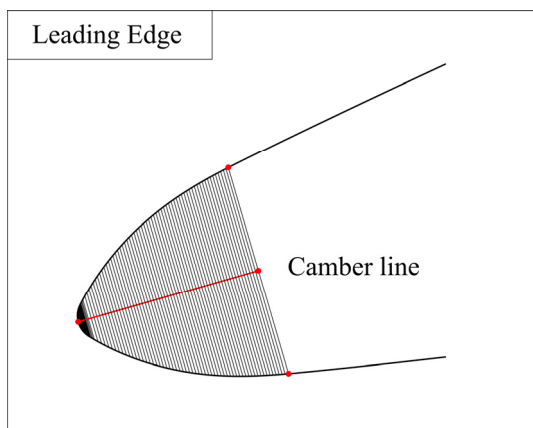
In this paper, as shown in Figure 2, the suction surface of the blade is fitted by using two Bezier curves, which connect smoothly at the position of the maximum blade thickness. The pressure surface is parametrized in the same way. For the leading edge of the blade, its thickness distribution is parametrized by using a Bezier curve with its camber line being a straight line, because the shape of the leading edge plays a very important role in the surface pressure distribution and the performance of the transonic cascade [10]. In the optimization, Points S1, S7, P1 and P7 are fixed. The degrees and directions of the movement of all other control points are shown by the arrows. The initial coordinates of the control points were obtained by fitting the initial blade profile. The trailing edge kept its profile throughout the optimization process.

The suction and pressure surface were fitted by two third-order Bezier curves, respectively. In contrast, a fourth-order Bezier curve was used to control the thickness distribution for the leading edge with the camber line keeping a straight line. Here, it should be pointed out that the changes in the positions of L2 and L4 can be determined by the angles of α_1 and α_2 . In the optimization, the control variables were α_1 and α_2 , which were used to control the thickness change rates at the starting point of the blade leading edge and at Point S1.

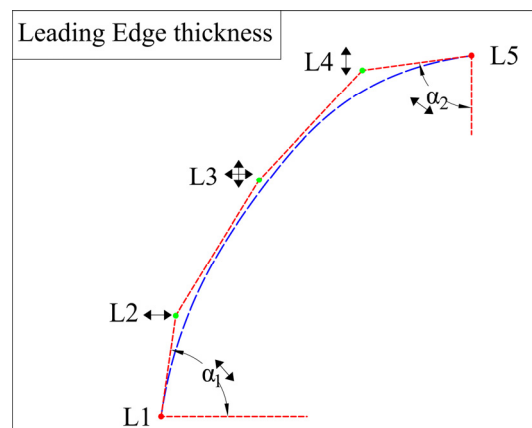
Furthermore, the tangent at Point S1 was determined by the profile of the leading edge, and the control point S2 should move along the tangent. It should be mentioned here that Point S3 moved along the horizontal line S3–S5 and did not lie on the extension line of S1–S2. In the same way, the second half of the suction surface could be determined. The same fitting strategy applied to the pressure surface.



(a)



(b)



(c)

Figure 2. Bezier curves and control points of the blade profile. (a) Control points for the suction surface and pressure surface; (b) leading edge; (c) leading edge thickness control points.

2.3. Numerical Method

In this paper, the ANSYS® Fluent was used to solve the flow field. The steady Reynolds-averaged Navier-Stokes (RANS) equations coupled with a turbulent model were solved by using the finite volume method. The two-dimensional (2D) steady-state simulations in double precision were conducted to optimize the cascade. In contrast, the three-dimensional (3D) steady-state simulations were carried out to simulate the experimental cascade flow field. The steady, three-dimensional (3D) RANS equations in the Cartesian coordinate system are expressed as follows [30]:

$$\frac{\partial \rho}{\partial t} + \frac{\partial(\rho U_j)}{\partial x_j} = 0 \tag{1}$$

$$\frac{\partial(\rho U_i)}{\partial t} + \frac{\partial(\rho U_i U_j)}{\partial x_j} = -\frac{\partial p}{\partial x_i} + \frac{\partial}{\partial x_j} \left[\mu \left(\frac{\partial U_i}{\partial x_j} + \frac{\partial U_j}{\partial x_i} \right) \right] \tag{2}$$

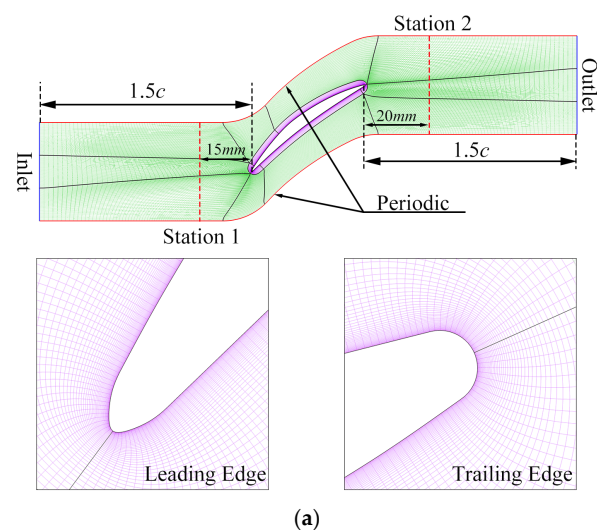
$$\frac{\partial(\rho h_t)}{\partial t} - \frac{\partial p}{\partial t} + \nabla(\rho U h_t) = \nabla(\lambda \nabla T) + \nabla(U \cdot \tau) \tag{3}$$

where ρ , U , p and T are the fluid density, velocity, pressure and temperature, respectively. The variable h_t is the total enthalpy of the fluid, and $\nabla(U \cdot \tau)$ represents the work due to viscous stresses. To close the control equations, the ideal gas state equation is also included:

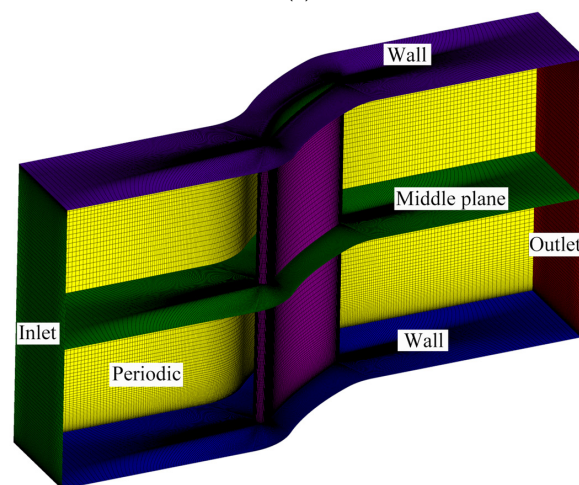
$$p = \rho RT \quad (4)$$

In order to capture the detailed flow field and analyze the internal flow loss mechanisms inside the transonic compressor cascade, the shear stress transfer (SST) $k-\omega$ model was chosen as the turbulence model, following the work of Huang et al. [12] and Ju and Zhang [22].

Figure 3 shows the grid topology for this transonic compressor cascade. As shown in Figure 3a, the computational domain is extended $1.5c$ upstream and downstream of the cascade. To improve the orthogonality of the grid, the H-O-H grid topology was used and a 60-layer grid was set within the blade boundary layer. The first grid layer next to the blade surface was set to $y^+ < 1$ to ensure the accuracy of the viscous fluid solution in the boundary layer. The 3D domain in Figure 3b is an extension of the 2D computational domain along the span direction with a span height of 100 mm, according to the experimental cascade size. The grid layer along the span is 120 and the total grid number for the 3D simulation is 6.53 million, with y^+ of the first layer next to the blade being less than 1, as shown in Figure 4.



(a)



(b)

Figure 3. Computational grid of the transonic compressor cascade. (a) Grid topology and the 2D grid; (b) 3D computational grid for the linear cascade.

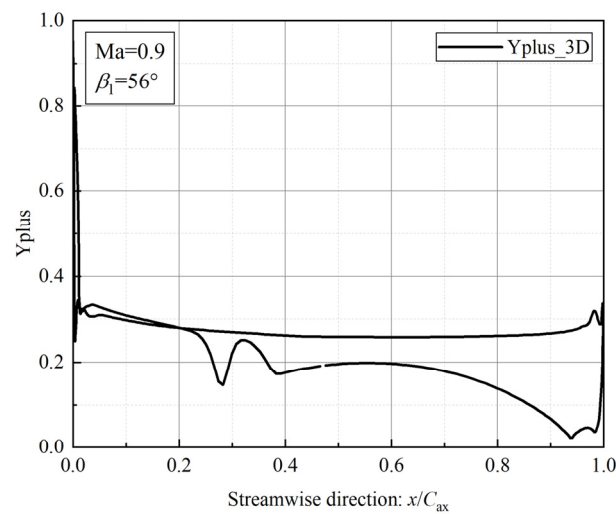


Figure 4. The blade wall y^+ distribution in the middle plane.

As for the boundary conditions, the pressure-far-field [3] was set at the inlet boundary with a given airflow direction; meanwhile, a pressure-out boundary condition was imposed at the outlet boundary. The turbulence intensity was set to 1% according to the wind tunnel data, and the turbulence length scale was given as the hydraulic diameter of the inlet section of the cascade. The periodic boundary condition was assigned to the side boundaries of the single blade passage. The blade surfaces and the end walls (for 3D computations) were given the adiabatic no-slip wall boundary condition. The main setups of the density-based solver and boundary conditions are summarized in Table 2.

Table 2. Solver settings and boundary conditions.

	2D	3D
Turbulence model	SST- $k\omega$	SST- $k\omega$
Solver type		Density-based
Working material		Ideal gas
Formulation		Implicit
Flux type		Roe-FDS
Inlet boundary conditions		pressure-far-field
Outlet boundary conditions		pressure-out

In the experiment [23], two stations referred to as Station 1 and 2 were used to measure the performance of the cascade, as shown in Figure 3. Station 1 was located 15 mm in the upstream of the leading edge while Station 2 was placed 20 mm downstream of the trailing edge of the blade, both along the axial direction. The cascade total pressure loss coefficient is defined as follows:

$$\omega = \frac{P_{t1} - P_{t2}}{P_{t1} - P_1} \quad (5)$$

where P_{t1} , P_{t2} and P_1 are the upstream total pressure, downstream total pressure and the upstream static pressure, respectively.

2.4. Grid Sensitivity Analysis and Numerical Method Validation

In this work, four grids for the 2D simulations and three turbulence models were adopted to verify the numerical model and independence of the grid. The number of 2D grid elements was increased from 30 k to 120 k. The variation in the total pressure loss coefficient with the 2D grid size is shown in Figure 5. When the element number is greater than 90 k, the total pressure loss coefficient almost becomes a constant. Therefore, the number of elements for the 2D simulation will remain at 90 k in the following optimization, to balance the computational accuracy and optimization efficiency.

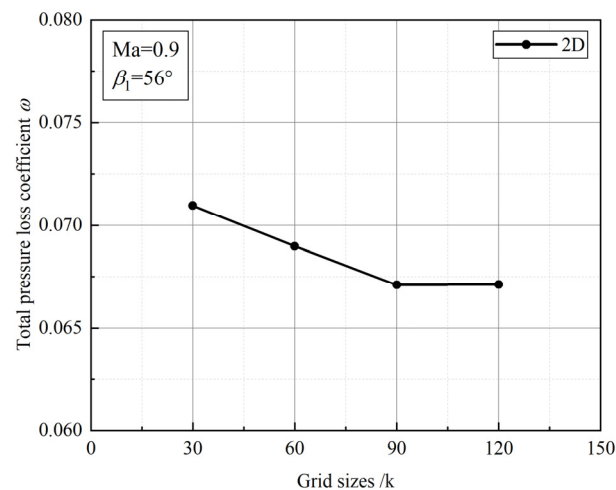


Figure 5. The variation in the total pressure loss coefficient with increased 2D grid sizes.

As for the turbulence models, the one-equation approach developed by Spalart and Allmaras (SA), the two-equation shear-stress transport $k\omega$ model ($k\omega$ -SST) and the four-equation transition SST model (also known as the γ - Re_θ model) were applied to the 3D grid. The CFD results were compared against the experimental data, which were obtained at an inlet Mach number of 0.9 with a midspan axial velocity density ratio (AVDR) of 1.48 in the wind tunnel. The pressure coefficient distribution comparison between the CFD and experimental results is shown in Figure 6. It can be seen that the CFD model based on the $k\omega$ -SST makes a reasonable prediction of the pressure distribution. So, the 2D and 3D flow simulations were carried out using the $k\omega$ -SST turbulence model. However, the experimental and CFD results do not agree well in the shock position ($x/C_{ax} = 0.2$ - 0.3). This is mainly due to the shock wave oscillation, which may smear the pressure jump measured by the pressure taps. For a detailed description, please refer to Ref. [29].

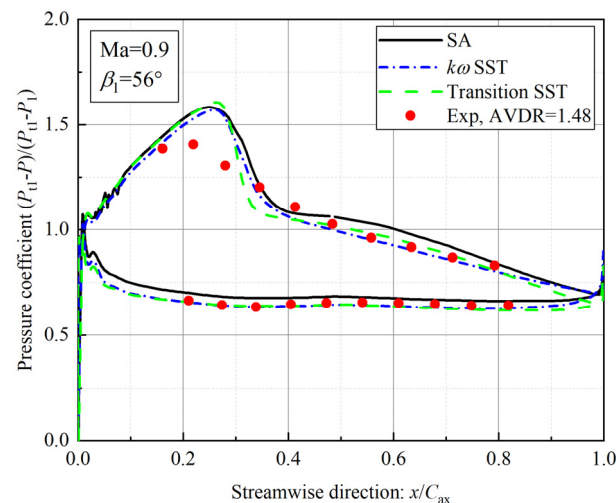


Figure 6. The blade surface pressure coefficient distribution with different turbulence models.

The pressure coefficient distribution comparison between the 2D and 3D results is shown in Figure 7. It can be seen that the difference between the 2D results and the experimental data is evident. However, the 3D calculation results agree well with the experimental results. This is because the 2D simulation could not take the influence of AVDR into consideration, while the 3D computation reveals the actual flow field information.

Therefore, the 3D computational results were used to analyze the underlying mechanisms for the reduction in flow losses. The pressure coefficient was defined as follows:

$$Cp = \frac{P_{t1} - P}{P_{t1} - P_1} \quad (6)$$

where P is the local static pressure on the blade surface.

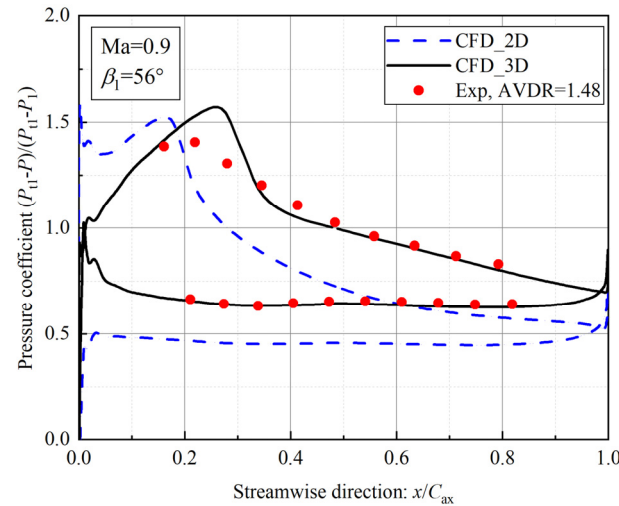


Figure 7. Pressure coefficient distribution comparison between 2D and 3D CFD results.

3. Cascade Optimization

3.1. Optimization Problem

The aim of this work was to reduce the total pressure loss coefficients of the cascade with the constraint of static pressure ratios, and to extend the cascade working range. The working range of the cascade is specified as the angle range in which the flow loss is less than two times the minimum loss coefficient in this paper. Therefore, the total pressure loss coefficients at three inlet airflow angles ($\beta_1 = 53^\circ$, $\beta_1 = 56^\circ$ and $\beta_1 = 58^\circ$) were chosen to form an optimization objective to achieve the aim of reducing flow losses and extending the working range simultaneously. The aerodynamic data at the three inlet flow angles are weighted equally, i.e., the optimization objective is the average of the flow losses at the three angles. In this way, the optimization of the flow losses at three different flow angles is transformed to a single-objective optimization problem.

3.2. Optimization Algorithm

The genetic algorithm (GA) is an optimization method to search for the optimal solution by simulating the natural evolutionary process [31]. Compared with the gradient optimization algorithm, it is easier to obtain the global optimal solution. In this paper, the GA is used to optimize the above proposed objective function.

To save the large number of expensive CFD simulations, the surrogate model was used in the optimization algorithm. Because the Kriging surrogate model is a well-accepted unbiased estimation model with both local and global statistical properties [25], the Kriging model was employed to construct the surrogate model for the optimization objective. The basis function of the Kriging surrogate model is defined as:

$$\psi^{(i)} = \exp\left(-\sum_{j=1}^k \theta_j |x_j^{(i)} - x_j^{P_j}|\right) \quad (7)$$

From the above equation, it is known that the key procedure is to estimate the values of the parameters θ and P . One way to do this is to choose θ and P to maximize the likelihood function of the observed data y . The likelihood function is given by:

$$L = \frac{1}{(2\pi\sigma^2)^{\frac{n}{2}} |\Psi|^{1/2}} \exp \left[-\frac{(y - 1\mu)^T \Psi^{-1} (y - 1\mu)}{2\sigma^2} \right] \tag{8}$$

where μ and σ are the mathematical expectation and standard deviation, respectively. The symbol Ψ represents the correlation matrix. By taking the natural logarithm of both sides of the above equation and taking the derivative of it, the concentrated log-likelihood function is obtained:

$$\ln(L) \approx -\frac{n}{2} \ln(\sigma^2) - \frac{1}{2} \ln|\Psi| \tag{9}$$

As a result, the function can be searched directly by GA. The value of this function depends on the unknown parameters θ and P . In this work, the model parameter $P = 2$ was fixed and only θ was adjusted. Moreover, it is meaningful to search for θ on a logarithmic scale, and a search range of 10^{-3} – 10^2 is appropriate. Additionally, the range of design variables was scaled to 0-1.

3.3. Optimization Process

The optimization process is summarized in the flowchart in Figure 8. It mainly comprises four modules: the DOE module, the blade geometry module, the CFD module and the optimization module.

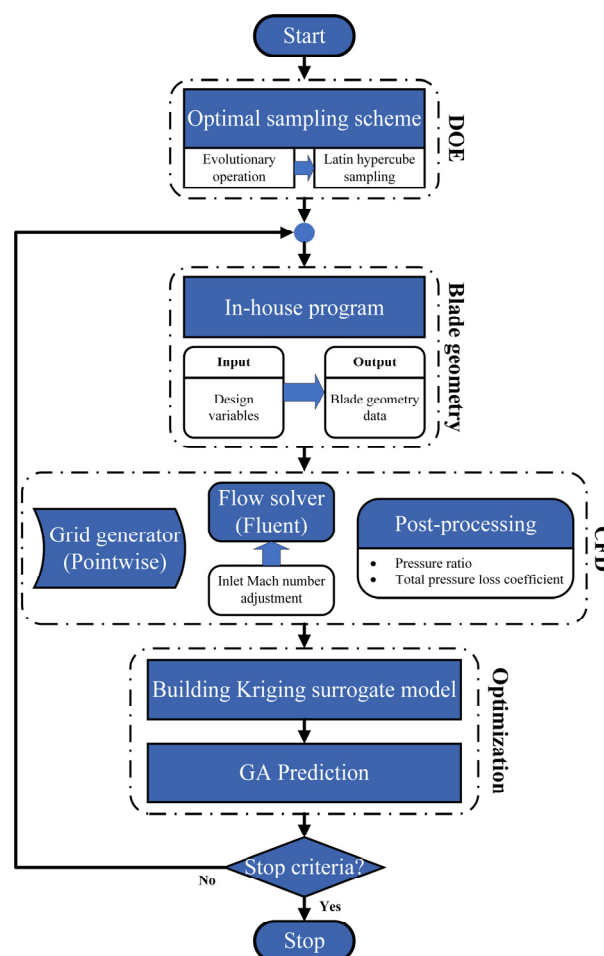


Figure 8. Flow chart of the transonic compressor cascade optimization process.

First, the design of experiment (DOE) method was chosen to be the Latin hypercube sampling (LHS). Two hundred optimally distributed sampling points were obtained for the optimization problem with 16 design variables using an in-house Matlab program, following the evolutionary operation for the LHS [32]. In the module of blade geometry, an in-house program was used to automatically produce the blade profile for simulations. In the CFD module, the back pressure needed to be interactively adjusted to make sure that the inlet Mach number was 0.9 in the numerical simulations at different airflow angles. For the detailed adjustment loop of the optimization, please refer to Ref. [18].

In the optimization module, an in-house Matlab program was used to build the surrogate model and the GA optimization algorithm. It is known that the surrogate model is just an approximate model of the real function to be optimized. In the optimization module, the surrogate model needed to be updated continually by adding new sampling points to the initial sampling group, to improve the model accuracy. In this work, the adding-point strategy of the maximum expected improvement criterion to improve the global accuracy of the model was adopted. This criterion combines both local excavation and global exploration to quickly obtain the exact optimal solution and improve the model global accuracy. In many situations, maximizing the expected improvement (EI) criterion has been shown to be the best strategy for finding the global optimal solution [33].

If the error function (erf) is used, the EI criterion is defined as follows:

$$E[I(x)] = (y_{\min} - \hat{y}(x)) \left[\frac{1}{2} + \frac{1}{2} \operatorname{erf} \left(\frac{y_{\min} - \hat{y}(x)}{\hat{s}\sqrt{2}} \right) \right] + \hat{s} \frac{1}{\sqrt{2\pi}} \exp \left[\frac{-(y_{\min} - \hat{y}(x))^2}{2\hat{s}^2} \right] \quad (10)$$

where \hat{y} and \hat{s}^2 are the mean value and variance, respectively. Moreover, in the process of optimizing the blade shape, the static pressure ratio of the cascade is required not to drop. Therefore, a surrogate model for the pressure ratio constraint is needed, except for the surrogate model for the objective function. Consequently, the adding-point criterion and the expected improvement method with consideration for the constraint were developed; the surrogate model for the constraint of pressure ratio was used to calculate the probability that the predicted pressure ratio was greater than the required value. The probability of a specific pressure range is defined as:

$$P[F(x)] = \frac{1}{\hat{s}\sqrt{2\pi}} \int_0^{\infty} e^{-(F-\hat{g}(x))^2/(2\hat{s}^2)} dG \quad (11)$$

where g is the constraint function and F represents the feasibility. The probability of satisfying the requirement of the constraint function was combined with the EI criterion of the objective function. The new adding-point criterion in the intersection set of the two surrogate models should satisfy the following expression, expressed as follows:

$$E[I(x) \cap F(x)] = E[I(x)]P[F(x)] \quad (12)$$

The objective function and constraint of the optimization problem are as follows:

$$\begin{cases} \text{Objective} = \min(\frac{\omega_1 + \omega_2 + \omega_3}{3}) \\ \text{Constraint} : \pi > \pi_{\text{original}} \end{cases} \quad (13)$$

where ω_1 , ω_2 and ω_3 correspond to the cascade total pressure loss coefficients at inlet airflow angles of 53° , 56° and 58° , respectively, and π_{original} is the mean value of the static pressure ratios at the three airflow angles.

4. Results and Discussion

The optimization of the compressor cascade was accomplished using the Kriging-model-based genetic algorithm. The optimal solution was obtained after 400 generations of evolution and about 600 rounds of CFD simulations. Three cases with a minimum total

pressure loss at the three specific airflow angles, named as Case 1, Case 2 and Case 3, were selected for the following analysis.

4.1. Comparison of Cascade Geometry and Overall Performance

First, the profiles of the initial blade and the optimization blades are shown in Figure 9. As can be seen, compared to the initial blade, the changes in the optimized blade profiles mainly occur in the first half of the blade. A first noticeable change is that the suction surface of the optimized blades becomes flatter and the radii of curvature of their pressure surface also increase, compared with the initial blade. Another interesting finding is that the maximum relative thicknesses of the optimized blades are all slightly increased, and their positions are also all shifted forward by roughly 10%, from nearly 54% chord length of the initial blade to nearly 45% chord length of the optimized blades. The quantitative comparison of the data is shown in Table 3. Another interesting finding is that the leading edges of the optimized blades become more ‘plump’ than that of the initial blade (see the zoomed-in figure). The underlying mechanism for the evolution trend of the blades of Case 1, Case 2 and Case 3 needs further exploration.

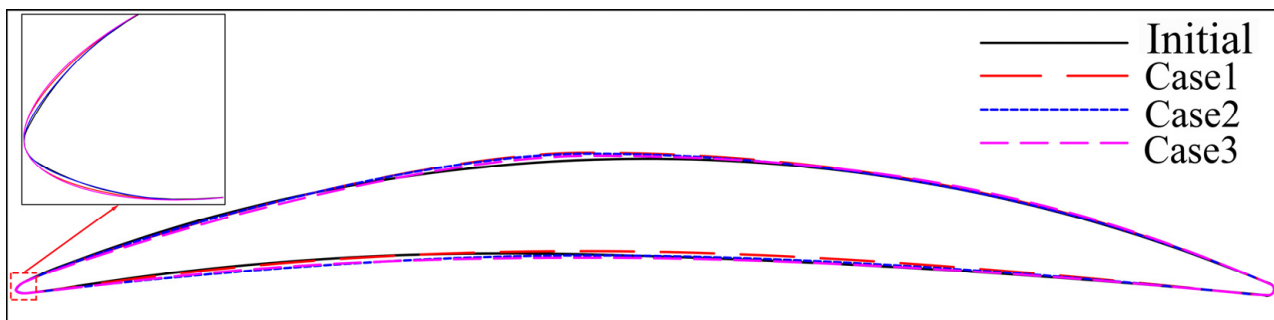


Figure 9. Comparison of geometric characteristics of cascade before and after optimization.

Table 3. Transonic compressor cascade design variables.

Variables	Initial	Case 1	Case 2	Case 3
Maximum relative thickness m/c	0.0785	0.0787	0.0813	0.0814
Relative maximum thickness position S_{4x}/c	0.5414	0.4541	0.4542	0.4567
Leading edge thickness distribution $\alpha_1(^{\circ})$	87.61	87.78	87.64	87.61
Leading edge thickness distribution $\alpha_2(^{\circ})$	19.76	19.59	19.11	20.56

To compare the cascade aerodynamic performance, 2D numerical simulations at different inlet airflow angles were performed for the initial cascade and the optimized cascades, as shown in Figure 10. It can be seen that three optimized cascades all have a lower loss coefficient compared to the initial cascade, and the static pressure ratio does not decrease in the working range. At the minimum loss point, the loss coefficient of Case 3 drops by 11% compared with that of the initial cascade. In addition, the working range of the optimized cascades is extended, increasing from 7.2° to 7.7° with a 6.9% improvement for Case 1, for example. The optimization results achieve our goal of reducing the flow loss and extending the working range.

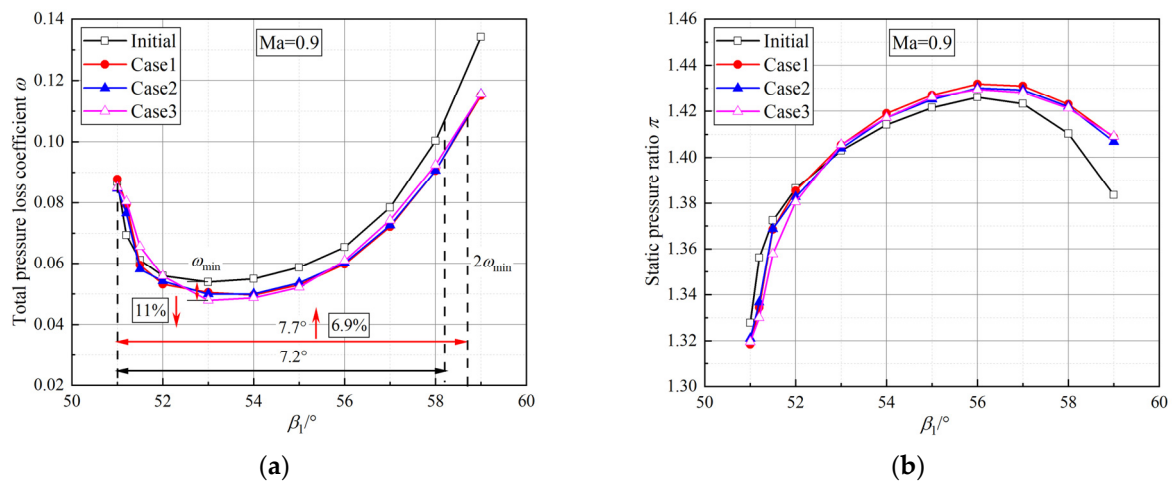


Figure 10. Comparison of the cascade performances. (a) Total pressure loss coefficients; (b) static pressure ratios.

4.2. Performance Improvement Mechanism

Considering the influence of AVDR on the cascade performance, a 3D numerical simulation at an inlet airflow angle of 56° was selected to analyze the mechanism for the cascade performance improvement. The flows in the middle plane were selected to make the comparison. The total pressure loss coefficient in the middle plane at the 56° inlet airflow angle is compared in Table 4. The total pressure loss coefficients of the optimized cascades are reduced by 9.4% (Case 1), 13.3% (Case 2) and 12.3% (Case 3), compared to the initial cascade.

Table 4. Comparison of the total pressure loss coefficient in the middle plane ($\beta_1 = 56^\circ$).

Case	ω	Relative Reduction %
Initial	0.058	/
Case 1	0.052	9.4
Case 2	0.050	13.3
Case 3	0.051	12.3

To explore the mechanism for the cascade performance enhancement, the pressure coefficient distributions in the middle plane of the 3D numerical results are illustrated in Figure 11. Obviously, the peak of the pressure coefficient of the initial cascade decreases evidently, which indicates that the shock strength becomes weak and the pre-shock Mach number drops. The forward movements of the blade maximum thickness and the change in the profiles of the optimized blades make the front half of the blades look more closely like wedge or 2D diffusers. This greatly reduces the maximum shock strength in the cascades. Additionally, the compressor blade often has a small ‘spike’ of the pressure distribution on the suction surface at the leading edge. The spike height is defined as the change in C_p from the peak to the trough of the spike (see the zoomed-in figure in Figure 11). Martin N and Robert J [34] pointed out that the performance of a cascade is not affected by the leading edge shape when the spike diffusion factor is kept below 0.1. The spike diffusion factor is defined in Eq. 14. From the pressure coefficient distribution at the leading edge, it can be seen that the suction surface spike heights of the optimized blades are higher than those of the initial blade. The spike diffusion factors are summarized in Table 5. According to the results of Ref. [34], if the spike diffusion factor exceeded 0.1, it would bring about a 30% rise in the profile loss of suction surface. This is mainly due to the fact that an increase in spike height leads to an increase in the energy thickness of the trailing edge boundary layer. In contrast, the optimized cascades all have a reduced total pressure loss coefficient

of the cascade (see Table 4), although their spike diffusion factors are all higher than the initial blade's. The reason for this needs detailed investigation.

$$D_{\text{spike}} = \frac{u_{\text{max}} - u_{\text{min}}}{u_{\text{max}}} \quad (14)$$

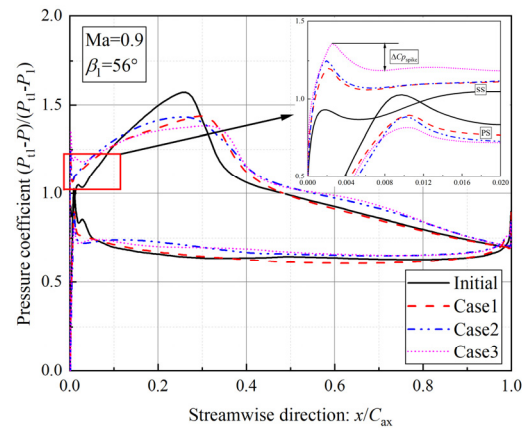


Figure 11. Distribution of the blade surface pressure coefficient in the middle plane.

Table 5. Comparison of the spike diffusion factor.

Case	D_{spike}
Initial	0.07
Case 1	0.11
Case 2	0.14
Case 3	0.12

It is worth noting that at the leading edge of the initial blade, the pressure coefficient curve of the pressure surface intersects with that of the suction surface (the zoomed-in figure in Figure 11). The Mach number contour at the leading edge reveals, as shown in Figure 12, that two high-speed cells appear next to the pressure surface of the initial blade, and this is the reason why there is an intersection of the two pressure coefficient curves. In contrast, the leading edges of the optimized cascades are plumper in shape than the initial cascade; therefore, the flow accelerates more quickly near the leading suction surface. This results in a higher spike height for the three cases at the leading edge (Figure 11). However, the optimized blade profiles counteract the possible increase in the momentum thickness in the boundary layer on the suction surface and the corresponding extra profile loss.

The transonic compressor cascade often has a shock wave in the blade passage. The interaction between the boundary layer and the strong shock wave can induce the boundary layer to separate from the blade, and results in an evidently increased flow loss [35]. Figure 13 shows the Mach number contour over the suction surface, where the black line is the sonic line ($Ma = 1$). It can be seen that the pre-shock Mach numbers of the optimized cascades decrease significantly, resulting in weaker passage shocks than that of the initial cascade. The shock pattern changes from a strong passage normal shock of the initial blade to a passage oblique shock. It is noticeable that the initial passage normal shock wave interacts with the boundary layer, resulting in boundary layer separation and a separation bubble (as shown in Figure 13). On the contrary, all of the optimized cascades do not have boundary layer separation, because the strength of the shock wave is evidently reduced. In order to quantitatively analyze the separation bubble induced by the shock boundary layer interaction, the distribution of the skin friction coefficient C_f on the suction surface is given in Figure 14. There is an obvious separation bubble on the blade suction surface. The separation bubble is located at the position of 30% chord length, and has a length of about 6.3% chord length. After optimization, the separation bubble induced by the shock wave

disappears for all of the optimized cascades. According to the above analysis, it is evident that although the shock loss and profile loss are difficult to be accurately distinguished, the benefit from the weakened shock strength is greater than the increased profile loss caused by the rising leading edge spike diffusion factor.

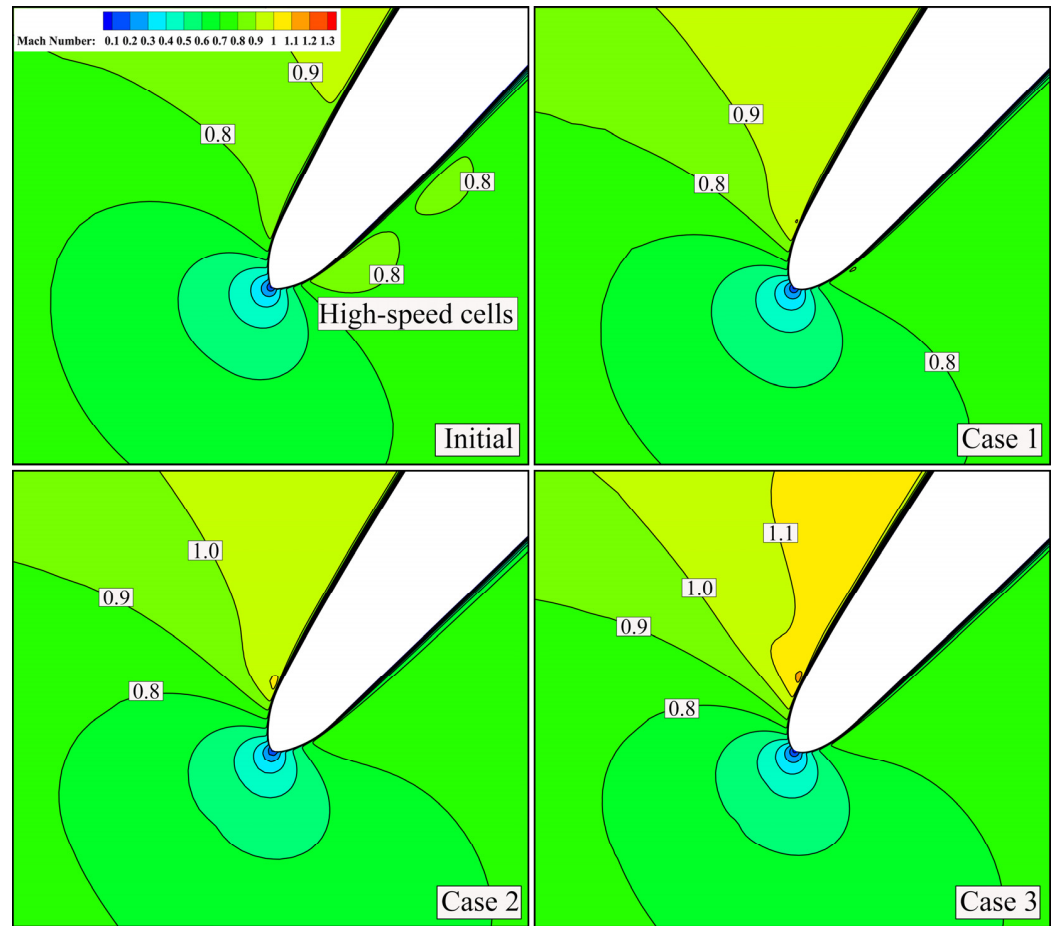


Figure 12. The Mach number contour of the leading edge in the middle plane.

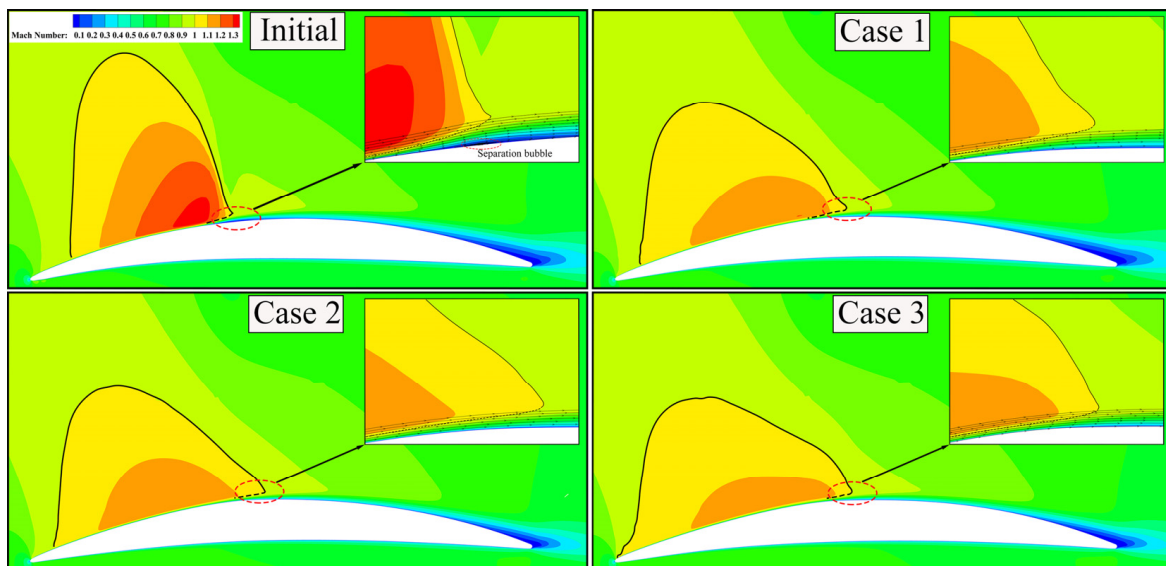


Figure 13. The Mach number contour of the suction surface in the middle plane.

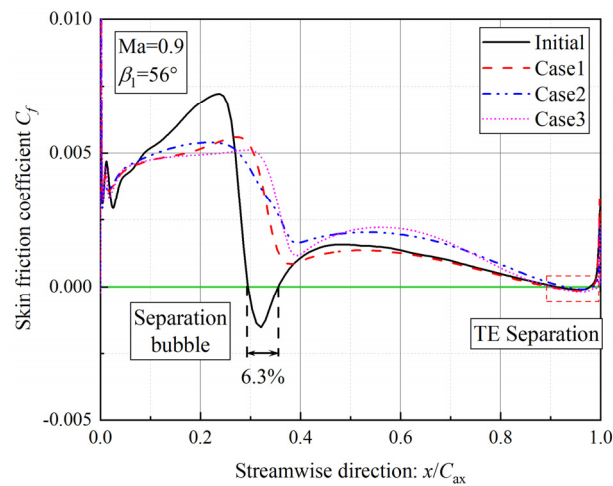


Figure 14. Distribution of the skin friction coefficient on the suction surface.

Figure 15 shows the total pressure loss coefficient at the position of Station 2 in the middle plane. It can be seen that the wake widths of the optimized cascade are all significantly reduced compared to the initial cascade. If the wake width is defined as the width at half of the depth [12], it is reduced from 28.8% of the pitch of the initial cascade to 17.5% (Case 1), 21.9% (Case 2) and 21.6% (Case 3), respectively, after optimization. Table 6 indicates that wake widths in the optimized cascades were reduced by 39.2%, 24.0% and 25% for Cases 1, 2 and 3, respectively, compared with the initial cascade. Moreover, the contours of the total pressure loss distribution on the cross section at Station 2 for the initial and optimized cascades are shown in Figure 16. Compared to the initial cascade, the results show that the high loss regions ($\omega > 0.45$) of the optimized cascades decrease considerably. It can be concluded that the optimized cascades perform better than the initial cascade, no matter whether they are 2D flows or 3D flows.

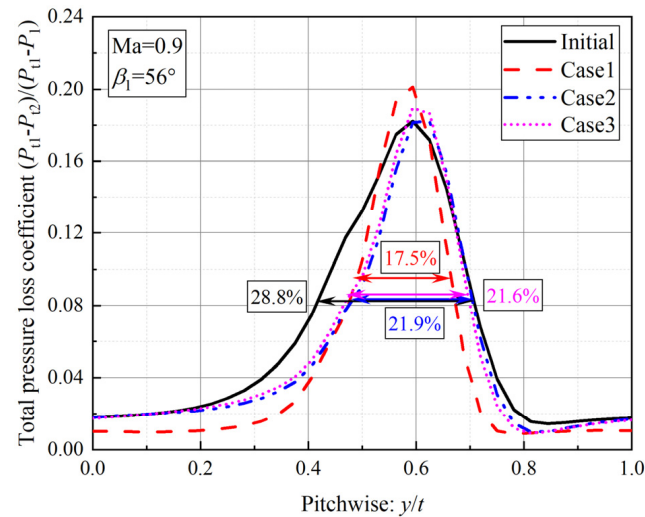


Figure 15. Total pressure loss coefficient distribution in the wake (middle plane).

Table 6. Comparison of the wake widths in the middle plane.

Case	Wake Width %	Relative Reduction %
Initial	28.8	/
Case 1	17.5	39.2
Case 2	21.9	24.0
Case 3	21.6	25

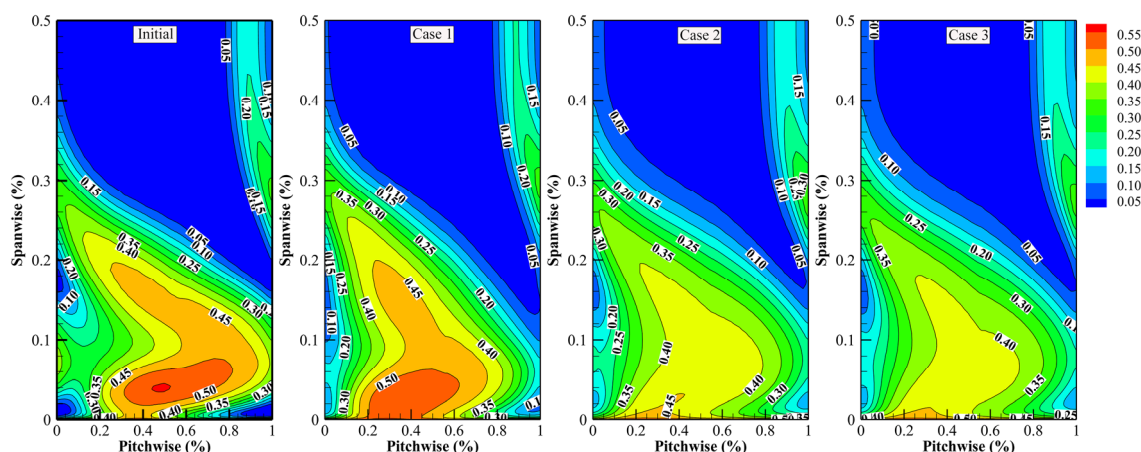


Figure 16. Comparison of the total pressure loss at outlet section (Station 2).

5. Conclusions

In this paper, a new blade parameterization method is proposed to construct the profile of the upper and lower surfaces and the leading edge of the transonic blade. A Kriging-assisted optimization method is proposed and used to optimize the cascade to reduce the total pressure loss and extend the working range. The main conclusions are as follows:

1. The blade parameterization method proposed in this paper has the advantages of using only 16 control variables to fit the blade profile precisely, covering the profiles of the suction surface, the pressure surface and the leading edge.
2. The proposed optimization method is an effective approach to be used to reduce the total pressure loss while extending the working range of the conventional transonic cascade with about 600 rounds of CFD simulations. For the 2D simulations, the total pressure loss coefficient of the optimized cascades has a nearly maximum reduction of 11% at the best flow angle and the working range is extended by 6.9%, compared to the initial cascade. For the 3D simulations, the total pressure loss coefficients of the optimized cascades decreased by 9.4% (Case 1), 13.3% (Case 2) and 12.3% (Case 3) at an inlet airflow angle of 56° , respectively.
3. It was found that the maximum thickness positions of the optimized cascades move forward by 10% toward the leading edges, and the radii of curvature of the suction and pressure surfaces increase as well, compared with the initial cascade. This makes the front half of the optimized blades look more like a wedge. Consequently, the optimized cascades have a lower pre-shock Mach number and a weakened shock strength, and the shock pattern changes from a passage normal shock to a passage oblique shock.
4. The evident separation bubble on the suction surface of the initial blade caused by the shock wave boundary layer interaction disappears on the optimized blades, due to the reduced shock strength. The weakened shock wave plays a more important role in performance improvement in the optimized transonic compressor cascades than other factors, such as the increase in the spike diffusion at the leading edge. The optimized cascades show better performance in both the 2D and 3D flow conditions.

Author Contributions: Conceptualization, F.M. and J.L.; methodology, F.M. and K.L.; software, C.G.; validation, F.M., K.L. and J.X.; formal analysis, F.M. and J.L.; investigation, F.M.; resources, F.M.; data curation, C.G.; writing—original draft preparation, F.M.; writing—review and editing, J.L. and P.G.; visualization, C.G.; supervision, J.X.; project administration, J.L.; funding acquisition, J.L. All authors have read and agreed to the published version of the manuscript.

Funding: This research was funded by National Science and Technology Major Project, grant number (2017-II-0007-0021).

Data Availability Statement: Not applicable.

Conflicts of Interest: The authors declare no conflict of interest. The funders had no role in the design of the study; in the collection, analyses, or interpretation of data; in the writing of the manuscript; or in the decision to publish the results.

References

1. Biollo, R.; Benini, E. Recent advances in transonic axial compressor aerodynamics. *Prog. Aerosp. Sci.* **2013**, *56*, 1–18. [[CrossRef](#)]
2. Gaitonde, D.V. Progress in shock wave/boundary layer interactions. *Prog. Aerosp. Sci.* **2015**, *72*, 80–99. [[CrossRef](#)]
3. Wang, Z.; Chang, J.; Li, Y.; Kong, C. Investigation of shock wave control by suction in a supersonic cascade. *Aerosp. Sci. Technol.* **2021**, *108*, 106382. [[CrossRef](#)]
4. Hergt, A.; Klinner, J.; Grund, S.; Willert, C.; Steinert, W.; Beversdorff, M. On the importance of transition control at transonic compressor blades. *J. Turbomach.-Trans. ASME* **2021**, *143*, 031007-1–031007-11. [[CrossRef](#)]
5. Koike, S.; Babinsky, H. Vortex generators for corner separation caused by shock-wave/boundary-layer interactions. *J. Aircr.* **2019**, *56*, 239–249. [[CrossRef](#)]
6. Titchener, N.; Babinsky, H. A review of the use of vortex generators for mitigating shock-induced separation. *Shock Waves* **2015**, *25*, 473–494. [[CrossRef](#)]
7. Mazaheri, K.; Khatibirad, S. Optimization of bump and blowing to control the flow through a transonic compressor blade cascade. *Shock Waves* **2018**, *28*, 285–297. [[CrossRef](#)]
8. Jinks, E.; Bruce, P.; Santer, M. Optimisation of adaptive shock control bumps with structural constraints. *Aerosp. Sci. Technol.* **2018**, *77*, 332–343. [[CrossRef](#)]
9. Wheeler, A.P.S.; Miller, R.J. Compressor wake/leading-edge interactions at off design incidences. In Proceedings of the Turbo Expo: Power for Land, Sea, and Air, Berlin, Germany, 9–13 June 2008.
10. Wheeler, A.P.S.; Sofia, A.; Miller, R.J. The effect of leading-edge geometry on wake interactions in compressors. *J. Turbomach.* **2009**, *131*, 041013. [[CrossRef](#)]
11. Wheeler, A.P.S.; Miller, R.J.; Hodson, H.P. The effect of wake induced structures on compressor boundary-layers. *J. Turbomach.* **2007**, *129*, 705–712. [[CrossRef](#)]
12. Huang, S.; Lu, X.; Han, G.; Zhao, S.; Zhou, C.; Yang, C. Research on aerodynamic optimization design method and flow mechanism of a high-subsonic compressor cascade. *Eng. Appl. Comput. Fluid Mech.* **2022**, *16*, 316–334. [[CrossRef](#)]
13. Steinert, W.; Eisenberg, B.; Starcken, H. Design and testing of a controlled diffusion airfoil cascade for industrial axial flow compressor application. *J. Turbomach.* **1991**, *113*, 583–590. [[CrossRef](#)]
14. Kulfan, B.; Bussoletti, J. “Fundamental” parametric geometry representations for aircraft component shapes. In Proceedings of the 11th AIAA/ISSMO Multidisciplinary Analysis and Optimization Conference, Portsmouth, VA, USA, 6–8 September 2006.
15. John, A.; Shahpar, S.; Qin, N. Alleviation of shock-wave effects on a highly loaded axial compressor through novel blade shaping. In Proceedings of the Turbo Expo: Power for Land, Sea, and Air, Seoul, Republic of Korea, 13–17 June 2016.
16. Walther, B.; Nadarajah, S. Adjoint-based constrained aerodynamic shape optimization for multistage turbomachines. *J. Propuls. Power* **2015**, *38*, 1–22. [[CrossRef](#)]
17. Ju, Y.; Zhang, C. Multi-objective optimization design method for tandem compressor cascade at design and off design conditions. In Proceedings of the Turbo Expo: Power for Land, Sea, and Air, Glasgow, UK, 14–18 June 2010.
18. Meng, F.; Li, K.; Guo, P.; Wang, K.; Li, J. Multi-objective shape optimization of transonic compressor cascade at the same inlet Mach number. *J. Chin. Inst. Eng.* **2022**, *45*, 465–475. [[CrossRef](#)]
19. Koeller, U.; Mo¨nig, R.; Ku¨sters, B.; Schreiber, H.A. 1999 Turbomachinery Committee Best Paper Award: Development of advanced compressor airfoils for heavy-duty gas turbines—Part I: Design and optimization. *J. Turbomach.* **2000**, *122*, 397–405. [[CrossRef](#)]
20. Burguburu, S.; le Pape, A. Improved aerodynamic design of turbomachinery bladings by numerical optimization. *Aerosp. Sci. Technol.* **2003**, *7*, 277–287. [[CrossRef](#)]
21. Ju, Y.P.; Zhang, C.H. Multi-point and multi-objective optimization design method for industrial axial compressor cascades. *Proc. Inst. Mech. Eng. Part C J. Mech. Eng. Sci.* **2011**, *225*, 1481–1493. [[CrossRef](#)]
22. Venturelli, G.; Benini, E. Kriging-assisted design optimization of S-shape supersonic compressor cascades. *Aerosp. Sci. Technol.* **2016**, *58*, 275–297. [[CrossRef](#)]
23. Cravero, C.; Marogna, N.; Marsano, D. A numerical study of correlation between recirculation length and shedding frequency in vortex shedding phenomena. *WSEAS Trans. Fluid Mech.* **2021**, *16*, 48–62. [[CrossRef](#)]
24. Shi, L.; Yang, G.; Yao, S. Large eddy simulation of flow past a square cylinder with rounded leading corners: A comparison of 2D and 3D approaches. *J. Mech. Sci. Technol.* **2018**, *32*, 2671–2680. [[CrossRef](#)]
25. Jeong, S.; Murayama, M.; Yamamoto, K. Efficient optimization design method using kriging model. *J. Aircr.* **2005**, *42*, 413–420. [[CrossRef](#)]
26. Wilson, B.; Cappelleri, D.; Simpson, T.W.; Frecker, M. Efficient pareto frontier exploration using surrogate approximations. *Opt. Eng.* **2001**, *2*, 31–50. [[CrossRef](#)]

27. Yue, S.; Wang, Y.; Wang, H. Design and optimization of tandem arranged cascade in a transonic compressor. *J. Therm. Sci.* **2018**, *27*, 349–358. [[CrossRef](#)]
28. Zhu, Y.J.; Ju, Y.P.; Zhang, C.H. An experience-independent inverse design optimization method of compressor cascade airfoil. *Proc. Inst. Mech. Eng. Part A-J. Power Energy* **2019**, *233*, 431–442. [[CrossRef](#)]
29. Meng, F.; Li, K.; Li, J.; Gan, J. Experimental and numerical studies of shock-wave boundary layer interactions in a highly loaded transonic compressor cascade. *J. Therm. Sci.* **2022**; *submitted*.
30. Abadi, A.M.E.; Sadi, M.; Farzaneh-Gord, M.; Ahmadi, M.H.; Kumar, R.; Chau, K.-W. A numerical and experimental study on the energy efficiency of a regenerative heat and mass exchanger utilizing the counter-flow maisotsenko cycle. *Eng. Appl. Comput. Fluid Mech.* **2020**, *14*, 1–12. [[CrossRef](#)]
31. Katoch, S.; Chauhan, S.S.; Kumar, V. A review on genetic algorithm: Past, present, and future. *Multimed. Tools Appl.* **2021**, *80*, 8091–8126. [[CrossRef](#)]
32. Box, G.E. Evolutionary operation: A method for increasing industrial productivity. *J. R. Stat. Soc. Ser. C* **1957**, *6*, 81–101. [[CrossRef](#)]
33. Jones, D.R. A taxonomy of global optimization methods based on response surfaces. *J. Glob. Optim.* **2001**, *21*, 345–383. [[CrossRef](#)]
34. Goodhand, M.N.; Miller, R.J. Compressor Leading Edge Spikes: A New Performance Criterion. *J. Turbomach.-Trans. ASME* **2011**, *133*, 021006. [[CrossRef](#)]
35. Babinsky, H.; Harvey, J. *Shock Wave-Boundary-Layer Interactions*; Cambridge University Press: Cambridge, NY, USA, 2011; pp. 87–136.

Disclaimer/Publisher’s Note: The statements, opinions and data contained in all publications are solely those of the individual author(s) and contributor(s) and not of MDPI and/or the editor(s). MDPI and/or the editor(s) disclaim responsibility for any injury to people or property resulting from any ideas, methods, instructions or products referred to in the content.